The 32nd International Congress and Exposition on Noise Control Engineering
Jeju International Convention Center, Seogwipo, Korea,
August 25-28, 2003

[N975] Patch near-field acoustical holography using a new statistically optimal method

Jørgen Hald
Innovations, R&D, Brüel & Kjær Sound & Vibration Measurement A/S,
Skodsborgvej 307, DK-2850 Danmark
jhald@bksv.com

ABSTRACT

The spatial FFT processing used in Near-field Acoustical Holography (NAH) makes the method computationally efficient, but it introduces severe spatial windowing effects, unless the measurement area is significantly larger than the source.
A Statistically Optimal NAH (SONAH) method is introduced which performs the plane-to-plane calculations directly in the spatial domain. Thereby the need for a representation in the spatial frequency domain and for zero padding is avoided, and spatial windowing effects are significantly reduced. The present paper describes the SONAH algorithm and presents some results from numerical simulations and practical measurements.
KEYWORDS: Near-field Acoustical Holography, Array Signal Processing, Windowing

INTRODUCTION

A plane-to-plane propagation of a sound field away from the source can be described mathematically as a 2D spatial convolution with a propagation kernel. A 2D spatial Fourier transform reduces this convolution to a simple multiplication by a transfer function. In Near-field Acoustical Holography (NAH) the Fourier transform is implemented as a spatial FFT of the pressure data measured over a finite area.
The use of spatial FFT and multiplication with a transfer function in the spatial frequency domain is computationally very efficient, but it introduces some errors. The discrete representation in the spatial frequency domain introduces periodic replica in the spatial

domain, causing "wrap-around errors" in the calculation plane. A standard way of pushing the replica away from the real measurement area is to use zero padding, which will however introduce a sharp spatial window. Such a window causes spectral leakage in the spatial frequency domain, which will show up as "window effects" in the calculation plane, [1]. As a consequence, the measurement area must be significantly larger than the source to avoid very disturbing window effects. This is a problem for example in connection with Time Domain NAH, [2], and Real-time NAH, which do not allow the synthesis of a large measurement area through scanning. The new Statistically Optimal NAH (SONAH) method performs the plane-to-plane transformation directly in the spatial domain rather than going via the spatial frequency domain, [3].

THEORY OF SONAH

The derivation of the SONAH algorithm given in this section is an extension of the derivation given in reference [4]. It is different from and probably simpler than the one given in reference [3].

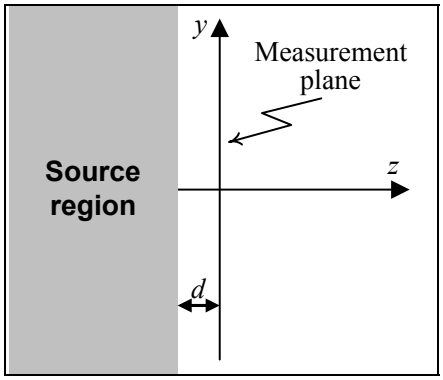

Figure 1. Geometry

We consider a complex, time-harmonic sound pressure field $p(\mathbf{r}) = p(x, y, z)$ with frequency f and wave number $k = \omega/c = 2\pi/\lambda$ where $\omega = 2\pi f$ is the angular frequency, c is the propagation speed of sound and λ is the wavelength. For the following description we shall assume that the half space $z \geq -d$ is source free and homogeneous, i.e. the sources of the sound field are for $z < -d$ as shown in Figure 1. The array measurements are performed in the plane $z = 0$.

From for example the theory of NAH, [1], it is well-known that the sound field for $z \geq -d$ can be written as an infinite sum of plane propagating and plane evanescent waves:

$$p(\mathbf{r}) = \frac{1}{(2\pi)^2} \int_{-\infty}^{\infty} \int_{-\infty}^{\infty} P(\mathbf{K})\ \Phi_{\mathbf{K}}(\mathbf{r}) d\mathbf{K} \tag{1}$$

Here, $\mathbf{K} \equiv (k_x, k_y)$ is a wave number vector, $P(\mathbf{K})$ is the Plane Wave Spectrum,

$$\Phi_{\mathbf{K}}(x, y, z) \equiv e^{-j(k_x x + k_y y + k_z (z+d))} \tag{2}$$

are plane propagating and plane evanescent wave functions, and the z-component k_z of the 3D wave number vector is the following function of $\mathbf{K}$:

$$k_z = k_z(\mathbf{K}) \equiv \begin{cases} \sqrt{k^2 - |\mathbf{K}|^2} & \text{for} \quad |\mathbf{K}| \le k \\ -j\sqrt{|\mathbf{K}|^2 - k^2} & \text{for} \quad |\mathbf{K}| > k \end{cases} \tag{3}$$

Notice that the elementary wave functions $\Phi_{\mathbf{K}}$ have identical amplitude equal to one on the source plane $z = -d$. The evanescent wave functions outside the Radiation Circle, i.e. for $|\mathbf{K}| > k$, are decaying exponentially away from the source. Since equation (1) has the form of an inverse spatial Fourier transform, the Plane Wave Spectrum P is a representation of the sound field in the spatial frequency domain.

We assume that the complex sound pressure $p(\mathbf{r}_n)$ has been measured at N positions $\mathbf{r}_n \equiv (x_n, y_n, 0)$ on the measurement plane. We wish to estimate the pressure $p(\mathbf{r})$ at an arbitrary position $\mathbf{r} \equiv (x, y, z)$ in the source free region $z \ge -d$, and we wish to estimate $p(\mathbf{r})$ as a linear combination of the measured sound pressure data $p(\mathbf{r}_n)$:

$$p(\mathbf{r}) \approx \sum_{n=1}^{N} c_n(\mathbf{r}) \cdot p(\mathbf{r}_n) \tag{4}$$

In order to determine the estimation coefficients c_n we require formula (4) to provide good estimation for a finite sub-set of the elementary wave functions of equation (2):

$$\Phi_{\mathbf{K}_m}(\mathbf{r}) \approx \sum_{n=1}^{N} c_n(\mathbf{r}) \cdot \Phi_{\mathbf{K}_m}(\mathbf{r}_n), \quad m = 1 \ldots M \tag{5}$$

Solution of this set of linear equations in a least squares sense means that we obtain the estimator (4) that is optimal for sound fields containing only the above function sub-set, and with approximately equal content of each function, i.e. with equal content of a set of spatial frequencies. Since all functions have amplitude equal to one on the source plane, the estimator is optimized for Plane Wave Spectra P, which are "white" in the source plane.

To solve (5) in a least squares sense we arrange the quantities in matrices and vectors:

$$\mathbf{A} \equiv \left[\Phi_{\mathbf{K}_m}(\mathbf{r}_n)\right] \quad \boldsymbol{\alpha}(\mathbf{r}) \equiv \left[\Phi_{\mathbf{K}_m}(\mathbf{r})\right] \quad \mathbf{c}(\mathbf{r}) \equiv \left[c_n(\mathbf{r})\right] \tag{6}$$

This allows (5) to be written as follows

$$\boldsymbol{\alpha}(\mathbf{r}) \approx \mathbf{A}\,\mathbf{c}(\mathbf{r}) \tag{7}$$

The regularized least squares solution to (7) is

$$\mathbf{c}(\mathbf{r}) = (\mathbf{A}^{\dagger}\mathbf{A} + \theta^2\mathbf{I})^{-1}\mathbf{A}^{\dagger}\boldsymbol{\alpha}(\mathbf{r}) \tag{8}$$

where $\mathbf{A}^{\dagger}$ is the conjugate transpose of $\mathbf{A}$, $\mathbf{I}$ is a unit diagonal matrix and θ is a regularization parameter. We now let the number M of elementary wave functions used to determine the estimation coefficients increase towards infinity, and we let the distribution of these wave functions in the $\mathbf{K}$ domain approach a continuous distribution:

$$\left[\mathbf{A}^{\dagger}\mathbf{A}\right]_{nn'} = \sum_{m} \Phi^*_{\mathbf{K}_m}(\mathbf{r}_n)\Phi_{\mathbf{K}_m}(\mathbf{r}_{n'}) \xrightarrow[m\to\infty]{} \frac{1}{\pi k^2}\iint \Phi^*_{\mathbf{K}}(\mathbf{r}_n)\Phi_{\mathbf{K}}(\mathbf{r}_{n'})\,d\mathbf{K} \tag{9}$$

$$\left[\mathbf{A}^{\dagger}\boldsymbol{\alpha}\right]_n = \sum_m \Phi^*_{\mathbf{K}_m}(\mathbf{r}_n)\Phi_{\mathbf{K}_m}(\mathbf{r}) \xrightarrow[m\to\infty]{} \frac{1}{\pi k^2}\iint \Phi^*_{\mathbf{K}}(\mathbf{r}_n)\Phi_{\mathbf{K}}(\mathbf{r})\,d\mathbf{K} \tag{10}$$

Here, * represents complex conjugate and the integration is over the 2D plane wave spectrum domain. Notice that the switch in (9-10) to integral representation introduces a re-scaling of the matrix $\mathbf{A}^{\dagger}\mathbf{A}$, which in turn necessitates a re-scaling of the regularization parameter θ.

The matrix $\mathbf{A}^{\dagger}\mathbf{A}$ can be seen as an Auto-correlation matrix for the set of measurement positions, while $\mathbf{A}^{\dagger}\boldsymbol{\alpha}$ can be seen as containing cross correlations between the measurement points and the calculation position.

The integrals in equations (9) and (10) can be reduced analytically by conversion of $\mathbf{K}$ to polar co-ordinates: $\mathbf{K} = (k_x, k_y) = (K\cos(\psi), K\sin(\psi))$. We introduce the *xy*-position vector $\mathbf{R} \equiv (x, y)$ and let $\mathbf{R}_n$ be the *xy*-component of $\mathbf{r}_n$. From (9) and (2) we get

$$\left[\mathbf{A}^{\dagger}\mathbf{A}\right]_{nn'} = \frac{1}{\pi k^2}\iint \Phi^*_{\mathbf{K}}(\mathbf{r}_n)\Phi_{\mathbf{K}}(\mathbf{r}_{n'})\,d\mathbf{K} = \frac{1}{\pi k^2}\iint e^{j(k_z^*-k_z)d} e^{j\mathbf{K}(\mathbf{R}_n-\mathbf{R}_{n'})}\,d\mathbf{K} \tag{11}$$

and further by polar angle integration and use of (3):

$$\begin{aligned}\left[\mathbf{A}^{\dagger}\mathbf{A}\right]_{nn'} &= \frac{1}{\pi k^2} 2\pi \int_0^{\infty} e^{j(k_z^*-k_z)d} J_0(KR_{nn'})\,KdK \\ &= 2k^{-2}\int_0^{k} J_0(KR_{nn'})\,KdK + 2k^{-2}\int_k^{\infty} e^{-2\sqrt{K^2-k^2}d} J_0(KR_{nn'})\,KdK \\ &= 2\frac{J_1(kR_{nn'})}{kR_{nn'}} + 2k^{-2}\int_k^{\infty} e^{-2\sqrt{K^2-k^2}d} J_0(KR_{nn'})\,KdK\end{aligned} \tag{12}$$

where $R_{nn'} \equiv \left|\mathbf{R}_n - \mathbf{R}_{n'}\right|$. Equation (10) can be treated in a similar way.

Clearly, all diagonal elements of the Autocorrelation matrix $\mathbf{A}^{\dagger}\mathbf{A}$ are identical because $R_{nn} = 0$ for all *n*, and the value can be shown to be:

$$\left[\mathbf{A}^{\dagger}\mathbf{A}\right]_{nn} = 1 + \frac{1}{2(kd)^2} \tag{13}$$

To solve for the vector $\mathbf{c}$ of prediction coefficients in equation (8), we need to choose the regularization parameter θ. It is shown in reference [3] that under some assumptions the optimal value is given by:

$$\theta^2 = \left(1 + \frac{1}{2(kd)^2}\right)\cdot 10^{-SNR/10} \tag{14}$$

where *SNR* is the effective Signal-to-Noise-Ratio in Decibel for the microphone signals, taking into account all sources of error.

We can now estimate the pressure at the position $\mathbf{r}$ through use of equation (4):

$$p(\mathbf{r}) \approx \sum_{n=1}^{N} c_n(\mathbf{r}) \cdot p(\mathbf{r}_n) = \mathbf{p}^{\mathrm{T}}\mathbf{c}(\mathbf{r}) = \mathbf{p}^{\mathrm{T}}(\mathbf{A}^{\dagger}\mathbf{A} + \theta^2\mathbf{I})^{-1}\mathbf{A}^{\dagger}\boldsymbol{\alpha}(\mathbf{r}) \tag{15}$$

Here, $\mathbf{p}$ is a vector containing the measured pressure signals, and we have used equation (8). Notice that the vector $\mathbf{p}^{\mathrm{T}}(\mathbf{A}^{\dagger}\mathbf{A} + \theta^2\mathbf{I})^{-1}$ of de-correlated pressure data over the microphone positions needs to be calculated only one time. After that it can be used for calculation of the pressure at many other positions $\mathbf{r}$ using other cross correlation vectors $\mathbf{A}^{\dagger}\boldsymbol{\alpha}(\mathbf{r})$.

The particle velocity can be obtained in the same way as a linear combination of the measured pressure signals. To derive the required estimation coefficients we start with an equation equivalent to (5), but with the particle velocity of the elementary wave functions on the left-hand side. As a result, we obtain the following expression for the particle velocity:

$$u_z(\mathbf{r}) \approx \mathbf{p}^{\mathrm{T}}(\mathbf{A}^{\dagger}\mathbf{A} + \theta^2\mathbf{I})^{-1}\mathbf{A}^{\dagger}\boldsymbol{\beta}(\mathbf{r}) \tag{16}$$

where $\mathbf{A}^{\dagger}\boldsymbol{\beta}$ is a vector of correlations between the pressure at the microphone positions and the particle velocity at the calculation position. Notice that the vector $\mathbf{p}^{\mathrm{T}}(\mathbf{A}^{\dagger}\mathbf{A} + \theta^2\mathbf{I})^{-1}$ of de-correlated measured pressure data from equation (15) applies also in equation (16).

Based on the sound pressure and the particle velocity, the sound intensity can be calculated.

NUMERICAL SIMULATIONS

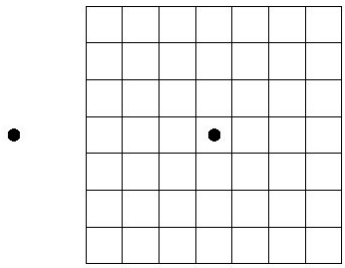

Figure 2. Microphone grid and point sources. The grid spacing is 3 cm and the two coherent point sources are 6 cm below the array. The left source is 6 cm to the left of the array.

A set of measurements was simulated with the set-up illustrated in Figure 2. Here, the grid represents an 8x8 element microphone array with 3 cm grid spacing, the microphones being at the corners of the grid. Two coherent in-phase monopole point sources of equal strength are positioned 6 cm below the array, i.e. at a distance that is two times the grid spacing. The positions of the point sources are indicated in Figure 2 by black dots. Clearly, the array does not cover the entire source area, so NAH will introduce severe spatial window effects. SONAH calculations were performed in the measurement plane (z=0) and in a plane half way between the source plane and the measurement plane (z=-3cm). The calculation grid had the same geometry as the measurement grid. The regularization parameter in equation (8) was set according to an *SNR* equal to 40 dB, and the source distance d was set to 6 cm.

First, the accuracy of the particle velocity estimation was investigated. For this, the central and the peripheral sections of the calculation area were considered separately, the peripheral section covering the 28 grid positions along the edges, and the central section covering the

rest. For each section/area the relative average error level was calculated from the formula:

$$L_{err} = 10 \cdot \log_{10} \left(\frac{\sum \left| u_i^{\text{true}} - u_i \right|^2}{\sum \left| u_i^{\text{true}} \right|^2} \right) \tag{17}$$

where the summations are both over the relevant section. A consequence of this definition is that a section with a low level of particle velocity will easier exhibit a high relative error level. Figure 3 shows the relative error levels in the measurement plane for the central area, for the edge and for the total area. For the central area the average relative error is seen to be lower than –18dB over the entire calculated frequency range from 500 Hz to 5 kHz.

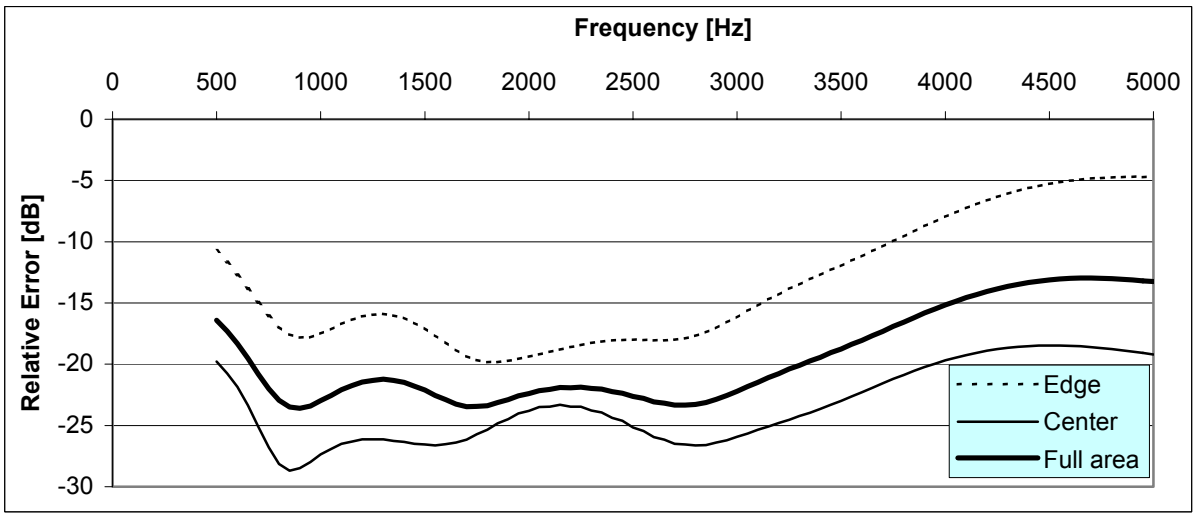

Figure 3. Relative average error level for SONAH calculation of particle velocity in the measurement plane, z=0.

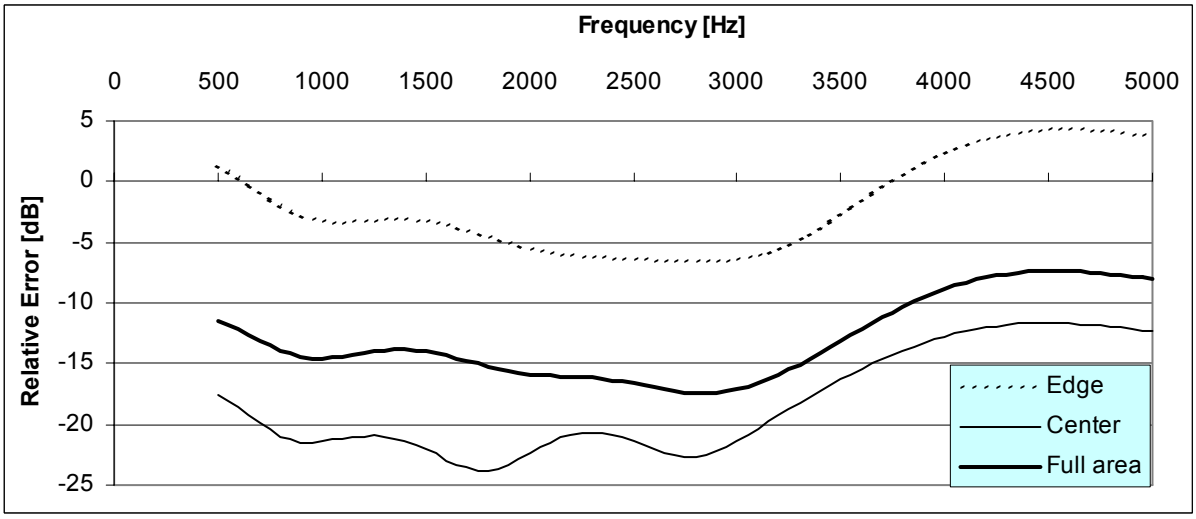

Figure 4. Relative average error level for SONAH calculation of particle velocity in the calculation plane at z=-3cm.

Figure 4 shows the corresponding data for the calculation plane at $z = -3$cm. Clearly, the error level has increased significantly, in particular along the edges, where the true particle velocity (z-component) is lower than before. The average error level over the central section/area is still better than around –18 dB up to 3.3 kHz and better than –12 dB up to 5 kHz.

Figure 5 shows the Sound Power for the central and for the full sections of the calculation area at $z = -3$cm. For both sections the sound power error is less than 0.2 dB up to around 3.5 kHz. Above that frequency the estimated power slowly gets too small, probably because the number of microphones is too small to uniquely determine general sound fields in that frequency range.

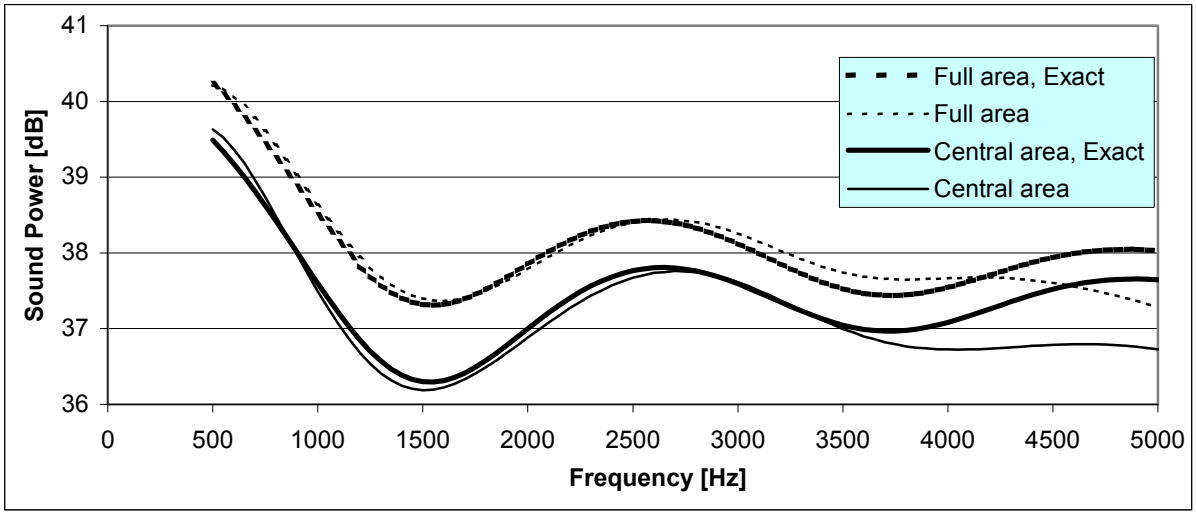

Figure 5. True and estimated sound power for the central and the full sections of the calculation area at $z = -3$cm.

PRACTICAL MEASUREMENT

The SONAH calculation method has been implemented in Brüel & Kjær's Non-Stationary STSF software package, which is an implementation of Time Domain acoustical holography. Here, time histories of sound pressure must be measured simultaneously at all measurement positions. The holography calculations are performed through an FFT transform of the full time-section to be studied to the frequency domain, followed by NAH or SONAH calculation for each FFT line and finally inverse FFT transform back to the time domain, [2]. In order to reduce the calculation time for the SONAH calculations, matrix interpolation was performed along the frequency axis on the correlation matrices $\mathbf{A}^{\dagger}\mathbf{A}$, $\mathbf{A}^{\dagger}\boldsymbol{\alpha}$ and $\mathbf{A}^{\dagger}\boldsymbol{\beta}$. With a few further efforts to reduce computation time, the SONAH calculations took only a few times longer than traditional NAH (based on spatial FFT processing) for the applied 120-element array.

The example to be presented here was a measurement on the side of the steel track of a large Caterpillar track-type tractor. The main sources of sound radiation were around the areas where the track passes over the sprocket and around the rear and front idlers. We took a measurement with a 10 cm spaced 10x12 element array positioned over a small Carrier Roller with a relatively low level of noise radiation. Figure 6 shows a picture of the measurement area and plots of the A-weighted, time-averaged (RMS) particle velocity maps for the frequency band 205-1454 Hz (1/12 octave bands). Clearly, SONAH has a much better ability to suppress spatial window effects than the traditional NAH technique.

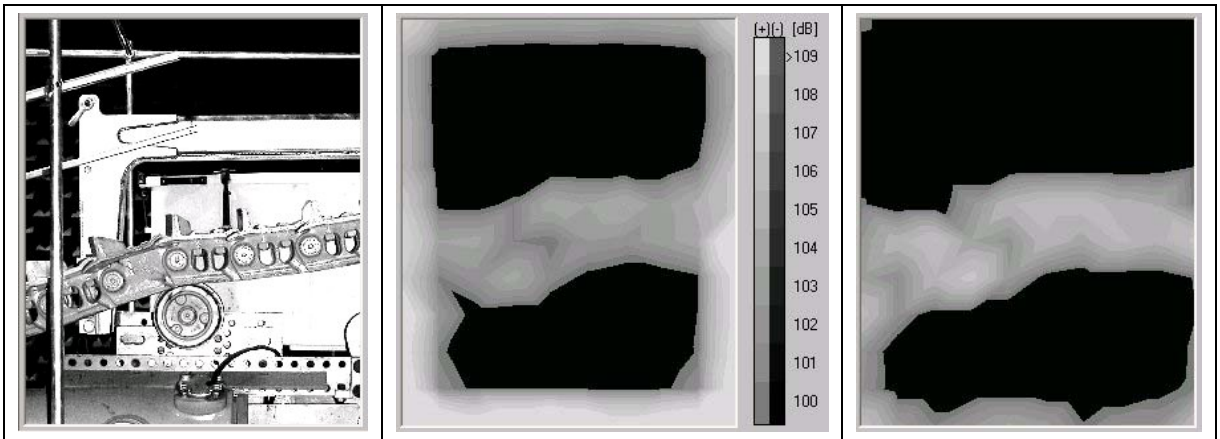

Measurement area | *NAH calculation* | *SONAH calculation*

Figure 6. Averaged Particle Velocity maps for the 1/12-octave bands 205-1454 Hz, A-weighted.

SUMMARY

The new Statistically Optimal NAH (SONAH) method has been introduced. This method performs the plane-to-plane transformation directly in the spatial domain, avoiding the use of spatial FFT. Careful numerical programming ensures calculation times only a few times longer than FFT based NAH. Numerical simulations and practical results demonstrate that SONAH opens up a possibility to perform acoustical holography measurements with an array that is smaller than the source, and still keep errors at an acceptable level.

REFERENCES

1. J.D. Maynard, E.G. Williams & Y. Lee, *J.Acoust.Soc.Am.*, **78**(4), 1395–1413, October 1985.
2. J. Hald, "Time Domain Acoustical Holography and Its Applications", *Sound & Vibration*, 16-25, February 2001.
3. R. Steiner & J. Hald, "Near-field Acoustical Holography without the errors and limitations caused by the use of spatial DFT", Proceedings of ICSV6, 1999.
4. J. Hald, "Planar Near-field Acoustical Holography with arrays smaller than the sound source", Proceedings of ICA 2001.